Acta Pharmaceutica Sinica B 2021;11(3):823–834

Chinese Pharmaceutical Association
Institute of Materia Medica, Chinese Academy of Medical Sciences

Acta Pharmaceutica Sinica B

www.elsevier.com/locate/apsb
www.sciencedirect.com

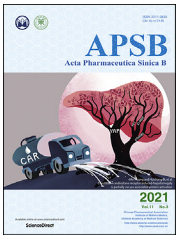

ORIGINAL ARTICLE

A smart MnO_2-doped graphene oxide nanosheet for enhanced chemo-photodynamic combinatorial therapy *via* simultaneous oxygenation and glutathione depletion

Peng Liu[a], **Xin Xie**[b], **Miao Liu**[a], **Shuo Hu**[c,d], **Jinsong Ding**[a], **Wenhu Zhou**[a,b,d,*]

[a]*Xiangya School of Pharmaceutical Sciences, Central South University, Changsha 410013, China*
[b]*School of Pharmaceutical Sciences, Gannan Medical University, Ganzhou 341000, China*
[c]*Department of Nuclear Medicine, Xiangya Hospital, Central South University, Changsha 410008, China*
[d]*Key Laboratory of Biological Nanotechnology of National Health Commission, Changsha 410008, China*

Received 12 May 2020; received in revised form 19 July 2020; accepted 21 July 2020

KEY WORDS

Cisplatin;
Nanoparticles;
Photosensitizer;
Tumor microenvironment;
Oxygenation;
GSH depletion;
Nanozyme;
Targeting

Abstract The combination of chemotherapy and photodynamic therapy provides a promising approach for enhanced tumor eradication by overcoming the limitations of each individual therapeutic modality. However, tumor is pathologically featured with extreme hypoxia together with the adaptable overexpression of anti-oxidants, such as glutathione (GSH), which greatly restricts the therapeutic efficiency. Here, a combinatorial strategy was designed to simultaneously relieve tumor hypoxia by self-oxygenation and reduce intracellular GSH level to sensitize chemo-photodynamic therapy. In our system, a novel multifunctional nanosystem based on MnO_2-doped graphene oxide (GO) was developed to co-load cisplatin (CisPt) and a photosensitizer (Ce6). With MnO_2 doping, the nanosystem was equipped with intelligent functionalities: (1) catalyzes the decomposition of H_2O_2 into oxygen to relieve the tumor hypoxia; (2) depletes GSH level in tumor cells, and (3) concomitantly generates Mn^{2+} to proceed Fenton-like reaction, all of which contribute to the enhanced anti-tumor efficacy. Meanwhile, the surface hyaluronic acid (HA) modification could facilitate the targeted delivery of the nanosystem into tumor cells, thereby resulting in amplified cellular toxicity, as well as tumor growth inhibition in nude mice model. This work sheds a new light on the development of intelligent nanosystems for synergistic combination therapy *via* regulating tumor microenvironment.

---

*Corresponding author.
E-mail address: zhouwenhuyaoji@163.com (Wenhu Zhou).

Peer review under responsibility of Chinese Pharmaceutical Association and Institute of Materia Medica, Chinese Academy of Medical Sciences.

https://doi.org/10.1016/j.apsb.2020.07.021

1. Introduction

Chemotherapy still remains the most prevailing means to treat cancer, and cisplatin (CisPt) is a widely used first-line chemotherapeutic drug. While most drugs display potent cytotoxicity both *in vitro* and *in vivo*, their long-term administration would inevitably provoke unwanted side-effects and acquired drug resistance[1]. To mitigate this deficiency, various combination strategies have been attempted to synergize the therapeutic efficacy[2−4]. Among them, the photodynamic therapy (PDT) has gained significant interest[5−9]. PDT is performed by photosensitizers to convert molecular oxygen into cytotoxic reactive oxygen species (ROS) upon laser irradiation, which causes oxidative damage to intracellular constituents and thus elicits cell death[10]. Due to the different anti-tumor mechanisms, PDT could effectively compensate chemotherapy by overcoming the limitations of each single therapeutic modality, thus reducing the drug doses and achieving the synergistic effects[11−15]. However, despite significant efforts on this front, the therapeutic outcomes of chemo-photodynamic combinations are still sub-optimal, which is partially restricted by the heterogeneity and complexity of tumor microenvironment[16,17]. In addition, due to the intrinsic polar structure of CisPt and its distinct physiochemical properties from most photosensitizers, it still remains a challenge to develop a co-delivery system for effectively combining CisPt and PDT.

In tumor tissue, extreme hypoxia is the characteristic pathological feature that restricts the therapeutic efficacy of oxygen-dependent PDT[18,19], and the situation becomes even worse upon PDT treatment as molecular oxygen is rapidly consumed to further exacerbate the hypoxia, leading to compromised efficacy and poor prognosis[20−22]. Towards this issue, we and other research groups have developed various combinatorial systems to relieve the tumor hypoxia for enhanced PDT efficiency by, for example, oxygen delivery, self-oxygenation and regulating tumor microenvironment[8,23−26]. On the other hand, tumor cells utilize ROS scavenging mechanisms to resist "oxidation therapy" such as PDT and even chemotherapy. Compared to normal cells, tumor cells display relative high oxidative stress because of the metabolic aberrations and dysfunctional redox regulation[27]. To improve this oxidative status and reduce oxidative damage, tumor cells activate several ROS scavenging pathways, including glutathione (GSH), catalase, superoxide dismutases (SOD) and vitamins[28−30]. Among them, GSH is the most abundant intracellular anti-oxidant species, which significantly hampers the PDT efficacy[31,32].

In addition, the overexpressed GSH in tumor cells is also employed to detoxify the chemotherapy *via* several mechanisms, which causes drug resistance[30,33]. For example, CisPt can easily bind GSH, and the product loses the capability to enter the nucleus for DNA damage, resulting in CisPt detoxification[34]. To address this issue, GSH-resistant or GSH-depleting polymeric micelles have been developed for CisPt delivery[35,36]. Therefore, the tumor microenvironment with such hypoxia and high GSH expression posts a significant challenge for both chemotherapy and PDT. As such, it is hypothesized that, if tumor hypoxia and the GSH level can be concomitantly alleviated at tumor site, the therapeutic efficacy of chemo-photodynamic combinations would be significantly strengthened. So, it is highly desirable to develop a multi-functional chemo-photodynamic combinatorial therapy, based on a well-designed nanosystem that can achieve both goals.

Recently, 2D graphene oxide (GO) has been extensively used as drug loading carrier for nanomedicine owing to its large planar surface for efficient aromatic drug adsorption, as well as the abundance of functional groups (*e.g.*, hydroxyl and carboxyl groups) for drug conjugation and further modifications[37−41]. For example, the photosensitizer chlorin e6 (Ce6) was loaded onto GO *via* physisorption[42,43], and cisplatin was conjugated on GO *via* ester bond which facilitated the subsequent microRNA adsorption to realize gene−chemo combinations[44]. Herein, GO was exploited as the nano-delivery system to realize the co-delivery of CisPt and Ce6 (designated as GO/CisPt/Ce6). Specifically, CisPt was aquated and covalently attached on the edge of GO through the ester bond, and Ce6 was facilely adsorbed on the plane surface. To solve the bottlenecks of both chemotherapy and PDT, such co-delivery system was further decorated with MnO_2 nanoparticles on the 2D surface to form GO/CisPt/Ce6@MH. Note that this is the first example of metal oxide-doped GO nanosheet for *in vivo* drug delivery. The doped MnO_2 not only acted as a nanozyme to catalyze the decomposition of tumor abundant H_2O_2 into O_2 for self-oxygen supply and thus relieve the tumor hypoxia, but also exerted an effective GSH depletion effect by oxidation of GSH (Scheme 1). Meanwhile, the MnO_2 was reduced to Mn^{2+}, which became a Fenton reagent to generate toxic ROS using H_2O_2 as substrate for chemodynamic cancer therapy. It should be noted that Mn^{2+} is an essential element for physiological metabolism, so its homeostasis can be efficiently controlled by the biological system. In addition, the surface hyaluronic acid (HA) modification endowed the nanosystem with tumor recognition capability for targeted delivery. All solution, *in vitro*, and *in vivo* experiments have demonstrated the oxygenation and GSH depletion activities of the nanosystem, and the superior tumor ablation effect has been evidenced both *in vitro* and *in vivo*. Compared with previous reported chemo-photodynamic systems which require tedious preparation procedure or complicated materials engineering[45,46], our proposed nanosystem is advantageous for ease of preparation, and can realize one-stone-two-birds purpose endowed by MnO_2 dopping (*e.g.*, tumor hypoxia relief and GSH depletion), which is critical for enhanced CisPt/Ce6 combinatorial tumor therapy. This work provides a new solution to develop multi-functional drug delivery system for enhanced chemo-photodynamic combinatorial therapy.

2. Materials and methods

2.1. Materials

Cisplatin, manganese sulfate ($MnSO_4$), silver nitrate ($AgNO_3$) and 3-(4,5-dimethylthiazol-2-yl)-2,5-diphenyl tetrazolium bromide

(MTT) were provided by Sigma−Aldrich (Saint Louis, MI, USA). Graphene oxide (GO) was obtained from Nanjing XFNANO Materials Tech Co., Ltd. (Nanjing, China). Hyaluronic acid (HA, 7 kDa) was purchased from Lifecore Biomedical Company (Twin Cities, USA). Chlorin e6 (Ce6) was provided by Frontier Scientific, Inc (Logan, UT, USA), and 2′,7′-dichlorofluorescin diacetate (DCFDA) was obtained from Sinopharm Chemical Reagent Co., Ltd. (Shanghai, China). Live & dead viability/cytotoxicity assay was purchased from Invitrogen (New York, NY, USA), and 4′,6′-diamidino-2-phenylindole (DAPI) was purchased from Solarbio Biotech, Co., Ltd. (Beijing, China).

2.2. *Synthesis of GO/CisPt/Ce6@MH*

To synthesize aquated CisPt [Pt $(NH_3)_2(OH_2)_2]^{2+}$, 20 mg CisPt was mixed with 11.2 mg silver nitrate under vigorous stirring for 24 h[44]. Then, the mixture was centrifuged at 10,000×*g* for 10 min to remove the silver chloride byproduct, and then filtrated through 0.45 μm millipore filter to obtain the aquated CisPt. To prepare GO/CisPt/Ce6@MH, five mL aquated CisPt solution (40 μg/mL) was mixed with five mL graphene oxide (GO) solution (200 μg/mL) containing 10 mmol/L PBS (pH 7.4) for 1 h reaction in dark. Then, 42 μL Ce6 DMSO solution (6 mg/mL) was added and stirred for 24 h, followed by washing with ultrapure water to obtain CisPt and Ce6 co-loaded GO/CisPt/Ce6. Next, the GO/CisPt/Ce6 solution was sequentially added with 200 μL $MnSO_4$ (3.38 mg/mL) and 750 μL hyaluronic acid (20 mg/mL). Then, NaOH solution (1 mol/L) was applied to adjust the pH to 10, followed by 2-h reaction under vigorous stirring. Finally, the mixture was centrifuged and washed to obtain the GO/CisPt/Ce6@MH.

2.3. *Characterization of GO/CisPt/Ce6@MH*

The hydrodynamic size and zeta potential (ζ) were measured by dynamic light scattering (DLS) analysis using Malvern Zeta Sizer Nano series (Nano ZS, Malvern instruments, Malvern, UK). The morphology and elements distribution were determined by TEM-EDX instrument (Titan G2 60−300, FEI, Waltham, MA, USA). The thickness was examined by atomic force microscope (AFM, Bruker, Madison, Waltham, MA, USA). The surface elemental composition was examined by X-ray photoelectron spectroscopy (XPS, ThermoFisher-VG Scientific, ESCALAB250Xi, Madison, Waltham, MA, USA). The UV−Visible absorbance spectra were measured by UV−Visible spectrophotometer (UV2450, Shimadzu, Tokyo, Japan). The loading capacity (LC, %) of Ce6 was calculated by the Ce6 characteristic absorption peak at 404 nm using UV−Visible spectrophotometer. The LC (%) of CisPt on GO was determined using an ophenylenediamine (OPD) method[47].

2.4. *In vitro drug release behavior*

The release behavior of CisPt and Ce6 from GO/CisPt/Ce6@MH was examined by the centrifugation method. Briefly, GO/CisPt/Ce6@MH was suspended in dissolution medium (pH 5.5 and 7.4 PBS buffer, 10 mmol/L). The solution was shaken in a thermostatic shaker (100 rpm, 37 °C). The release medium was sampled (0.5 mL) at predetermined time intervals and centrifuged at 20,000×*g* for 20 min. The CisPt in the supernatant was analyzed by the OPD method and the Ce6 in the supernatant was determined from the characteristic absorbance peak at 404 nm.

2.5. *In vitro O_2 production and enhanced $^1O_2$ generation*

GO/CisPt/Ce6 or GO/CisPt/Ce6@MH (20 μg/mL) was added to the H_2O_2 solution (1 mmol/L), followed by monitoring the O_2 generation by using portable dissolved oxygen meter (JPBJ-609L, INESA Scientific Instrument Co., Ltd., Shanghai, China). The $^1O_2$ production was measured by using SOSG probe. Briefly, 0.8 mL of GO/CisPt/Ce6 or GO/CisPt/Ce6@MH (2 μg/mL Ce6) was dispersed into 0.1 mL SOSG solution (25 μmol/L), followed by

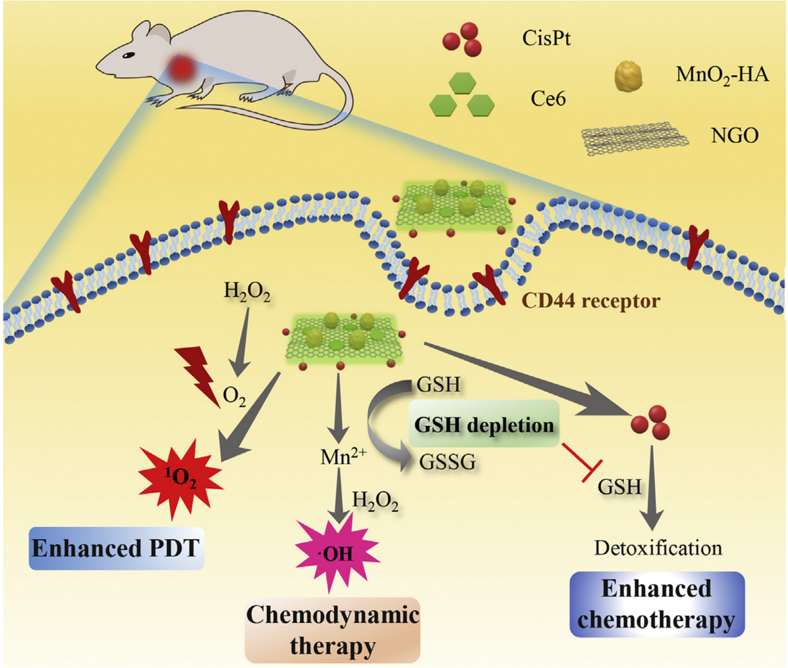

Scheme 1 Schematic illustration of GO/CisPt/Ce6@MH for enhanced chemotherapy and photodynamic therapy against tumors.

adding 0.1 mL H_2O_2 (100 mmol/L). At predetermined time intervals, a continuous laser (635 nm, 0.1 W/cm^2) was applied, and the green fluorescence of SOSG was detected by fluorescence spectrophotometer (Ex = 490 nm, Em = 525 nm).

2.6. GSH depletion by GO/CisPt@MH

The GSH depletion was measured by using Ellman's reagent (Solarbio Bioteh). In detail, GSH solution (250 μmol/L) was mixed with GO, GO/CisPt and GO/CisPt@MH (20 μg/mL), respectively. After 30 min incubation, the Ellman's reagent was added, and the absorbance spectrum was recorded with a wavelength from 350 to 500 nm. To investigate the GSH depletion inside cells, the MDA-MB-231 cells were seeded in 6-well plate and treated with GO, GO/CisPt or GO/CisPt@MH (100 μg/mL) for 4 h. After washing with PBS, the cells were harvested and lysed using the Triton-X 100 cell lysis buffer. Then, the samples were centrifuged at 6000×*g* for 5 min, and the GSH concentration was measured by the Ellman's reagent.

2.7. Detoxification of CisPt by GSH

GO/CisPt/Ce6@MH, GO/CisPt/Ce6 or CisPt solution (2 μg/mL CisPt) was mixed with different concentrations of GSH (0.1, 0.5, and 1 mmol/L). After 30 min incubation, the mixture was reacted with an OPD solution (12 mg/mL, dissolved in DMF), and the concentration of active CisPt was calculated based on the UV−Vis absorbance intensity at 703 nm.

2.8. Mn^{2+}-mediated fenton-like reaction

The ·OH-generating activity was investigated by methylene blue (MB). Briefly, GO/CisPt/Ce6@MH (100 μg/mL) was mixed with GSH (1 mmol/L) and incubated at 37 °C for 30 min. After centrifuging at 20,000×*g* for 20 min, $NaHCO_3$ solution (25 mmol/L), MB solution (10 μg/mL) and H_2O_2 (8 mmol/L) were added to the supernatant. Then, the mixture was incubated at 37 °C for 30 min, and the MB degradation was monitored by the UV−Vis absorbance change at 665 nm.

2.9. Cell culture

MDA-MB-231 and RLE-6TN cells were cultured in DMEM complete medium containing 10% FBS (GIBCO, USA), 1% penicillin/streptomycin (100 U/mL, Solarbio Bioteh), and digested with 0.25% trypsin−EDTA (Solarbio Bioteh).

2.10. Cellular uptake

MDA-MB-231 or RLE-6TN cells were seeded in 35 mm culture dish at a density of 2 × 10^5 per milliliter and cultured overnight. Then, the cells (with or without pre-incubation of 10 mg/mL free HA) were treated with free Ce6 or GO/CisPt/Ce6@MH for 2 h. After fixing with 4% paraformaldehyde and labeling with DAPI, the cells were imaged by a confocal fluorescence microscope (LSM780 NLO, Zeiss, Oberkochen, Germany). The Ogura procedure was performed to quantify the cellular uptake of Ce6[48]. Briefly, MDA-MB-231 cells or RLE-6TN cells were seeded in 6-well plate and treated as above mentioned. After washing with PBS, the cells were harvested using a cell scraper. Afterwards, the cell debris was dissolved in one mL sodium dodecyl sulfate (SDS, 2%) for 2 h incubation. Then, one mL NaOH (0.2 mol/L) was added to extract Ce6 for quantification by using a fluorescence spectrophotometer (Ex = 404 nm, Em = 663 nm).

2.11. Intracellular ROS generation

MDA-MB-231 cells were seeded in 24-well culture plate at a density of 10^5 per well. The cells (with or without pre-incubation of 10 mg/mL free HA) were treated with Ce6, GO/CisPt/Ce6 or GO/CisPt/Ce6@MH for 2 h. Then, the cells were washed 3 times with PBS and further incubated with DCFDA (10 μmol/L) for 30 min. After irradiating for 2 min (0.1 W/cm^2), the cells were observed by fluorescence imaging system (NIKON, Ti−S, Tokyo, Japan).

2.12. In vitro cytotoxicity studies

MDA-MB-231 cells were seeded in 96-well plate (5 × 10^3/well) for 24 h culturing at 37 °C. Thereafter, different formulations with gradient concentrations were added for 24 h incubation. After irradiating with a laser (0.1 W/cm^2) for 1 min and incubating for 24 h, the MTT (5 mg/mL, 20 μL) was added, followed by 4 h incubation. Afterwards, MTT was removed and 100 μL DMSO was added to dissolve the formazan crystals. Finally, the absorbance at 570 nm was recorded and the cell viability was calculated. The cell apoptosis was investigated using calcein AM/propidium iodide (PI) double staining kit (Sangon Biotech, Shanghai, China). The MDA-MB-231 cells were seeded in a 24-well plate at a density of 2 × 10^5 per well and treated with various formulations for 24 h. Then, the cells were irradiated with laser (0.1 W/cm^2) for 1 min and incubated for 24 h, followed by dual Calcein AM and PI staining for fluorescent imaging.

2.13. In vivo antitumor activity

All animal experiments were performed according to the Regulations for the Administration of Affairs Concerning Experimental Animals of China, and approved by the Ethics Committee for Research in Animal Subjects at Xiangya School of Pharmaceutical Sciences of Central South University, China. Female BALB/c nude mice (6 weeks) were subcutaneously injected with a suspension of MDA-MB-231 cells in PBS. When the volume of tumors reached ∼100 mm^3, the MDA-MB-231 tumor-bearing BALB/c mice were randomly assigned to four groups and intratumorally injected with PBS, GO/CisPt/Ce6+Laser, GO/CisPt/Ce6@MH, GO/CisPt/Ce6@MH + Laser, respectively, $n = 5$ per group, at Day 0 (100 μL, 0.5 mg/kg Ce6). The laser (0.1 W/cm^2, 5 min) was performed at 24 h post-injection. The body weight and tumor size (V) of each mouse were recorded every 2 days for 2 weeks to evaluate the antitumor activity. The tumor size was calculated using the formulae Eq. (1):

$$V = (\text{Length} \times \text{Width}^2)/2 \tag{1}$$

The major organs and tumors were isolated and collected from the euthanized mice for hematoxylin and eosin (H&E) staining at Day 14 after treatment. The GSH content in tumor tissues was measured using homogenization method. Briefly, the weighed tumor after different treatments was immersed in saline, and tumor homogenate solution was prepared by homogenizer. After centrifuging at 2500×*g* for 10 min, the GSH content in supernatant was measured using Ellman's reagent.

2.14. Immunofluorescence analysis

After treatments, the mice were sacrificed and tumors were surgically resected. Then, tumor tissues were fixed to prepare frozen sections slices. The slices were incubated with the HIF-1α antibody (mouse polyclonal to HIF-1α) and changed with the secondary antibodies conjugated with FITC. Next, the nuclei were counterstained with DAPI. Images were acquired by confocal fluorescence microscope (LSM780 NLO).

3. Results and discussion

3.1. The construction of GO/CisPt/Ce6@MH

The nanoplatform was stepwise prepared as illustrated in Fig. 1A. CisPt was aquated in presence of $AgNO_3$, which allowed for conjugation with GO through ester bond[44]. Then, Ce6 was physisorbed on GO through $\pi-\pi$ stacking, forming the dual-drug loading system of GO/CisPt/Ce6. Interestingly, the platination of GO facilitated the Ce6 adsorption with considerably higher loading capacity (Supporting Information Fig. S1A), which is likely due to the decrease of the negative charge after CisPt conjugation that alleviates the charge repulsion between GO and Ce6 (Fig. S1B). The drug loading (DL, %) for CisPt and Ce6 was calculated to be 7.7% and 3.1%, respectively. Then, Mn^{2+} was *in situ* oxidized on GO/CisPt/Ce6 plane surface to form MnO_2 nanoparticles under alkaline condition, which was stabilized by hyaluronic acid (HA). With drugs loading and MnO_2 deposition, the resulting GO/CisPt/Ce6@MH displayed an average dynamic size ~380 nm with ζ potential of −46.7 mV (Supporting Information Fig. S2). Such highly negative charge is preferable for colloidal stability and *in vivo* delivery[49].

The GO/CisPt/Ce6 showed a sheet-like morphology as characterized by transmission electron microscope (TEM, Fig. 1B), while a large number of small-size MnO_2 (~50 nm) were seen on GO/CisPt/Ce6@MH (Fig. 1C). From TEM-associated energy dispersive X-ray (EDX) element mapping, N, Pt and Mn were clearly observed in GO/CisPt/Ce6@MH (Fig. 1D, and Supporting Information Fig. S3), representing the component of Ce6, CisPt and MnO_2, respectively. The existence of Pt and Mn elements was further confirmed by the X-ray photoelectron spectroscopy (XPS, Supporting Information Fig. S4), and the content of MnO_2 on the surface of NGO was 5.4%. The AFM was also employed to characterize these 2D nanomaterials. Both GO/CisPt/Ce6 and GO/CisPt/Ce6@MH showed squared shape with ~1 μm each edge (Fig. 1E and F, Supporting Information Fig. S5). However, upon MnO_2 deposition, the thickness was significantly increased from 3 to 50 nm, which is consistent with the size of MnO_2 as observed by TEM (Fig. 1C). The colloidal stability of the nanosystem was investigated by monitoring the dynamic particle size and polydispersity index (PDI). The GO/CisPt/Ce6@MH was stable in aqueous solution for at least 15 days (Supporting Information Fig. S6A). After mixing with fetal bovine serum (FBS) containing cell culturing medium, the particle size was also unchanged for 48 h (Fig. S6B), indicating high stability for the biological applications.

Next, we studied the *in vitro* drug release profiles of CisPt and Ce6 from GO/CisPt/Ce6@MH (Fig. 1G and H). For CisPt, an obvious pH-dependent drug release was observed, where the drug was stably conjugated at pH 7.4 but progressively released at pH 5.5. The cumulative release of CisPt was 10% (pH 7.4) and 60% (pH 5.5), respectively, after 48 h incubation. This pH-responsive behavior can be attributable to the hydrolysis of ester bond between GO and CisPt under acidic condition. Since Ce6 was adsorbed mainly through aromatic stacking, its release was much less affected by pH, displaying a typical sustained-release profile at both pH 7.4 and 5.5 with accumulative release lower than 40% after 48 h. Of note, the release rate of Ce6 even decreased slightly at lower pH. This is likely due to the protonation of Ce6 at low pH to become positive charge, which is attracted by negatively charged GO and thus impedes its desorption.

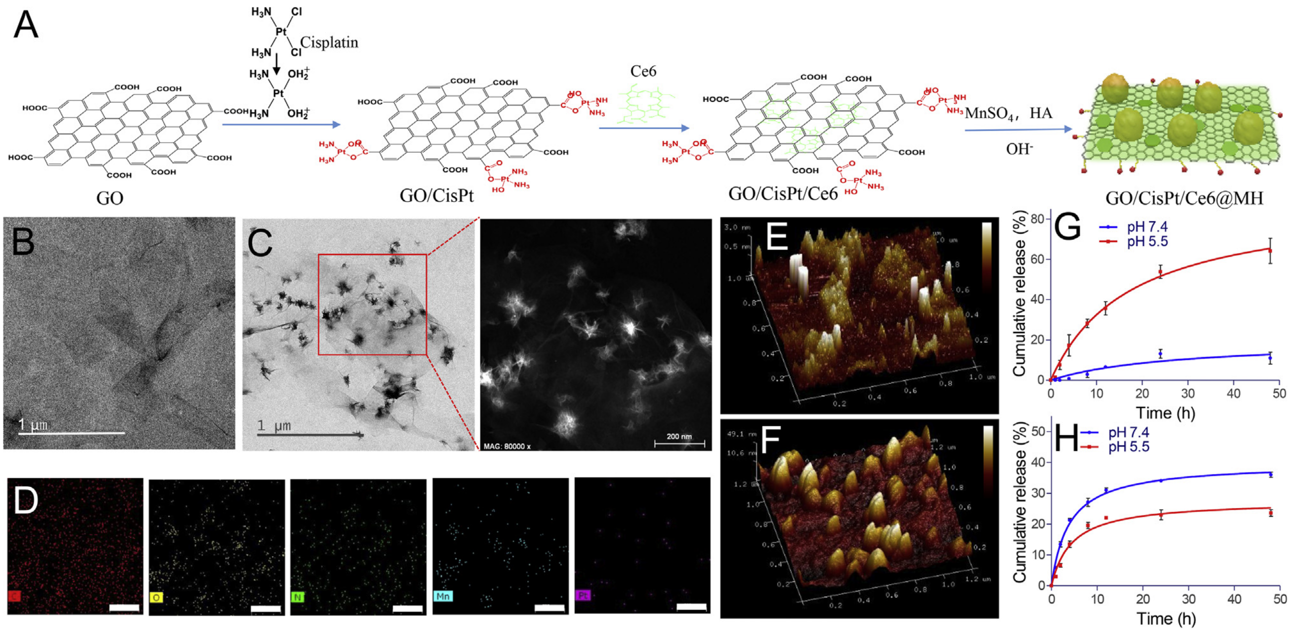

Figure 1 (A) The preparation process of GO/CisPt/Ce6@MH. TEM images of (B) GO/CisPt/Ce6 and (C) GO/CisPt/Ce6@MH (D) EDX elemental mapping of GO/CisPt/Ce6@MH, scale bar = 200 nm. AFM images of (E) GO/CisPt/Ce6 and (F) GO/CisPt/Ce6@MH. The *in vitro* drug release profile of (G) CisPt and (H) Ce6 from GO/CisPt/Ce6@MH. Data are expressed as mean ± SD (n = 4).

3.2. *Self-oxygen supply and GSH depletion by the doped MnO_2*

Then, the roles of MnO_2 on GO/CisPt/Ce6@MH were systematically evaluated. It is known that MnO_2 is a type of catalase-mimic nanozyme to catalyze the conversion of H_2O_2 into O_2, which has been widely used to relieve tumor hypoxia and sensitize PDT therapy by providing O_2 substrate[23,50,51]. To measure the catalytic activity, O_2 generation was investigated. GO/CisPt/Ce6@MH itself cannot produce O_2, while upon addition of H_2O_2, a large number of bubbles were observed in the tube (inset in Fig. 2A), indicating the O_2 generation. To quantify the reaction, the dissolved O_2 was monitored by the portable dissolved oxygen meter, and rapid O_2 production was detected within 100 s (Fig. 2A). For comparison, the combination of GO/CisPt/Ce6 and H_2O_2 failed to trigger O_2 production, confirming the catalytic activity of MnO_2. Such self-oxygen supply system was then explored for PDT enhancing capability by monitoring $^1O_2$ generation using the fluorescent SOSG probe. Upon exposure to laser, both GO/CisPt/Ce6 and GO/CisPt/Ce6@MH showed rapid $^1O_2$ production within 10 min (Fig. 2B). Notably, in presence of H_2O_2, GO/CisPt/Ce6@MH showed a considerably accelerated $^1O_2$ generation rate, verifying the advantage of MnO_2 for enhanced PDT therapy. Therefore, such self-oxygen supply platform can be used to strengthen PDT efficacy under H_2O_2 abundant conditions.

Another important function of MnO_2 is to regulate GSH concentration. GSH is the most abundant antioxidant inside cells, which protects cellular components from various ROS damages. For cancer therapy, however, GSH-mediated drug resistance presents a major challenge for various therapeutic modalities[35,52,53]. Therefore, an effective method for intracellular GSH depletion would be useful for enhancing the efficiency of chemo/PDT treatments. To measure the GSH regulation activity, we employed the probe of 5,5′-dithiobis-(2-nitrobenzoic acid) (DTNB)[54]. Free GSH can react with DTNB to form a yellow complex with a characteristic UV absorbance peak at 405 nm (Supporting Information Fig. S7). Therefore, the peak absorbance can be used for GSH quantification. Interestingly, with increasing GO/CisPt@MH concentration, the level of GSH gradually decreased (Supporting Information Fig. S8), suggesting a good GSH depletion activity. For comparison, GSH level was unchanged after GO/CisPt treatment (Fig. 2C). Therefore, the GSH depletion was indeed caused by MnO_2. Such GSH depletion activity was also confirmed in living cells by using MDA-MB-231 cancer cells. After 4 h incubation, GSH level was decreased by 20% (Fig. 2D).

After confirming the GSH depletion activity, we then tested the system for rescuing the GSH-mediated CisPt detoxification. GSH can inactivate CisPt through the formation of Pt—S bond (Supporting Information Fig. S9)[55], and after 30 min incubation 2 μg/mL CisPt was completed inactivated by 0.1 mmol/L GSH (Fig. 2E). Conjugation of CisPt on GO could prevent GSH-mediated inactivation to some extent, and this protection effect was further enhanced for GO/CisPt/Ce6@MH, due to the GSH depletion capability provided by MnO_2. All these results demonstrated the advantages of MnO_2 doping for sensitizing PDT therapy of Ce6 and enhancing chemotherapy of CisPt, thus

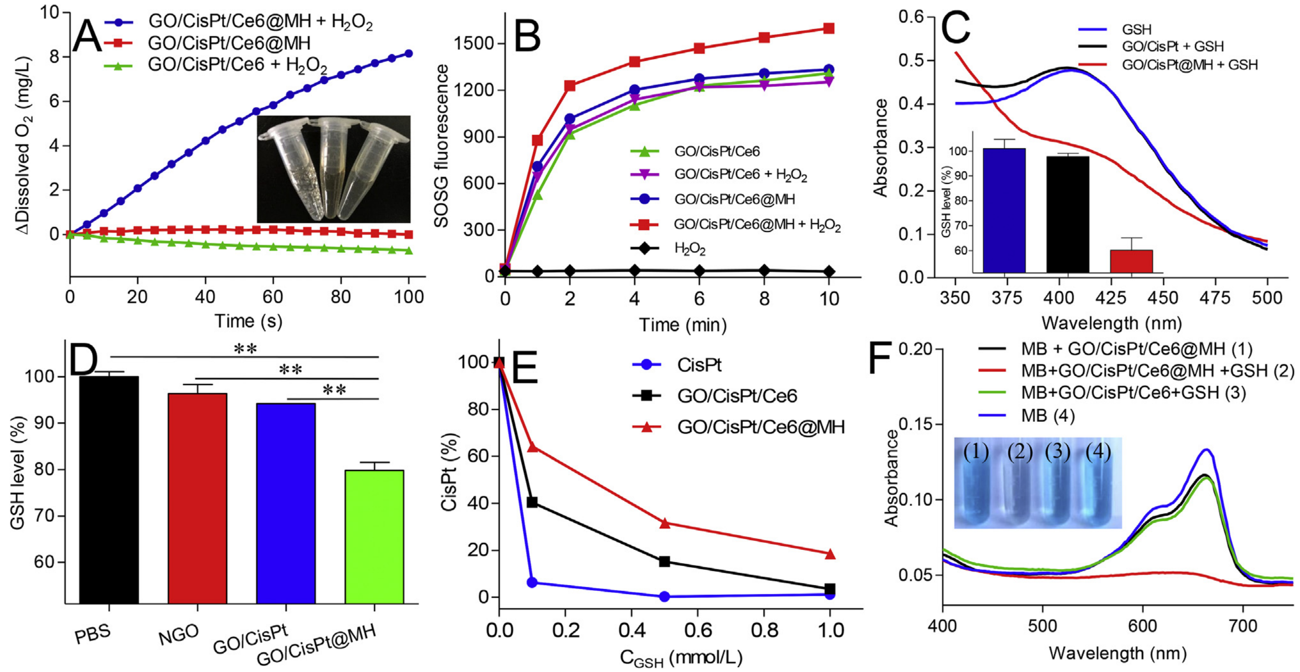

Figure 2 (A) The kinetics of O_2 generation catalyzed by GO/CisPt/Ce6 and GO/CisPt/Ce6@MH in presence or absence of 1 mmol/L H_2O_2. Inset: photographs of each reaction tube after reaction. (B) The kinetics of $^1O_2$ generation for GO/CisPt/Ce6 or GO/CisPt/Ce6@MH in the presence or absence of 1 mmol/L H_2O_2 under laser irradiation (C) UV—Vis absorbance spectra showing the GSH depletion activity for different formulations. Inset: the quantification of GSH depletion after incubating with various formulations for 30 min. (D) The GSH level in MDA-MB-231 cells after treatment with various formulations for 4 h. Data are expressed as mean ± SD ($n = 3$). $^{**}P < 0.01$. (E) The CisPt activity for free CisPt, GO/CisPt/Ce6 and GO/CisPt/Ce6@MH after incubating with different GSH concentrations for 30 min. Data are expressed as mean ± SD ($n = 3$). (F) UV—Vis absorbance spectra and photographs of MB after incubating with GO/CisPt/Ce6 or GO/CisPt/Ce6@MH in the presence or absence of 1 mmol/L GSH for 30 min.

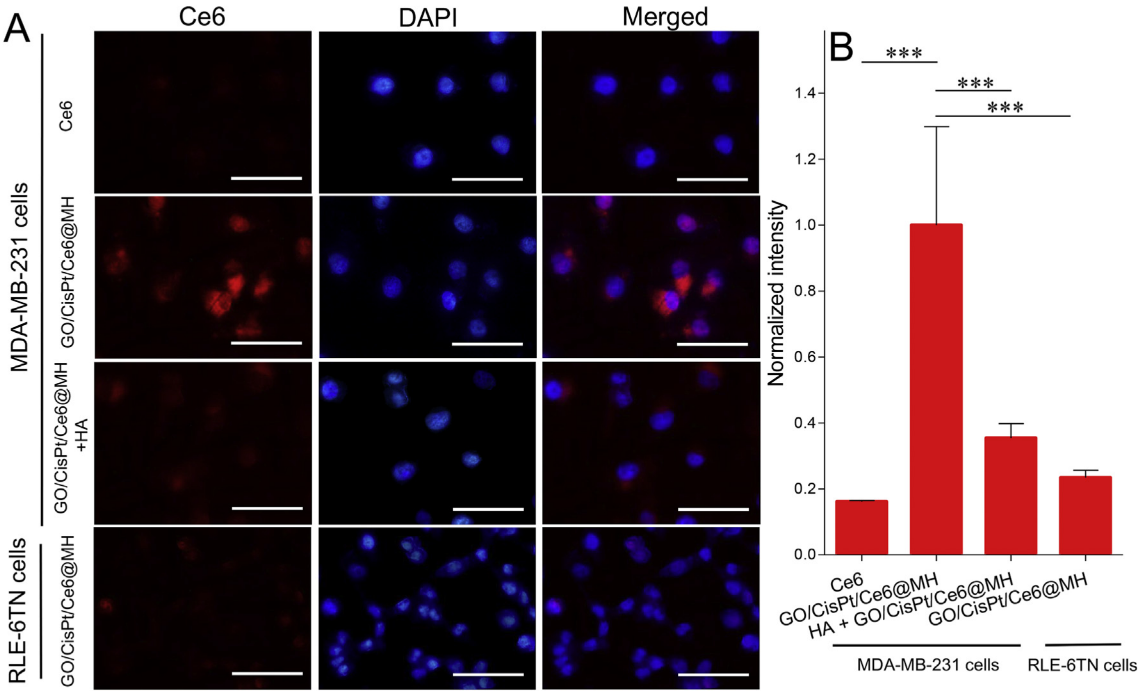

Figure 3 (A) Cellular uptakes of free Ce6 and GO/CisPt/Ce6@MH measured by CLSM. Scale bar = 50 μm. (B) Quantitative analysis of cellular uptake by Ogura method. Data are expressed as mean ± SD (n = 3). $^{***}P < 0.001$.

resulting in significantly enhanced therapeutic outcomes (*vide infra*).

Concomitant with GSH depletion, the MnO_2 was reduced to Mn^{2+}, which could act as an efficient Fenton reagent to catalyze the degradation of H_2O_2 in the presence of HCO_3^- to generate highly toxic ROS of ·OH for chemodynamic cancer therapy[56]. To investigate the Fenton-like reaction, we utilized the well-defined methylene blue (MB) as a colorimetric probe[57]. MB is an organic dyestuff that can be degraded by ·OH, accompanied by the decrease of characteristic UV absorbance peak at 665 nm. Free Mn^{2+} could decolorize the MB with completely disappearance of the characteristic absorbance, confirming the Fenton-like reaction (Supporting Information Fig. S10). We then tested the GO/CisPt/Ce6@MH. Without GSH, the nanosystem did not show Fenton activity (Fig. 2F). Upon addition of GSH, in contrast, an obvious Fenton-like MB degradation was observed both from the color change and UV absorbance decrease. In contrast, the GO/CisPt/Ce6 with GSH treatment failed to induce Fenton reaction. These results validate that GO/CisPt/Ce6@MH could release Mn^{2+} in response to GSH, which subsequently generates ·OH *via* Fenton-like reaction. Such ROS generation can be used for chemodynamic therapy to combine with PDT and chemotherapy, leading to multi-modal cancer therapy.

3.3. *Tumor targeted intracellular delivery*

Having confirmed the multi-functionalities of GO/CisPt/Ce6@MH, we next moved forward for the intracellular behaviors. First, the cellular uptake was studied. Since the surface of GO/CisPt/Ce6@MH was coated with a layer of HA, we expected that the nanosystem could specifically recognize cancer cells that overexpress CD44 receptor on cell membrane *via* the HA-CD44 interaction[58]. To explore the targeting efficiency, the MDA-MB-231 cancer cells line was chosen as a proof-of-concept, and normal cell line of RLE-6TN cells (low CD44 expression) was used as a control. The cells nuclei were stained blue by DAPI for localization, and the traffic of GO/CisPt/Ce6@MH was visualized by the intrinsic red fluorescence of Ce6. From confocal laser scanning microscopy (CLSM), the cells with free Ce6 treatment barely showed any red fluorescence, indicating minimal assimilation (Fig. 3A). This is likely due to the negatively charged Ce6 that is repelled by cell membrane. For GO/CisPt/Ce6@MH group, on the other hand, bright red fluorescence was observed inside cells after 2 h incubation, suggesting substantial uptake. However, the uptake efficiency of GO/CisPt/Ce6@MH by RLE-6TN cells was much lower. Therefore, the GO/CisPt/Ce6@MH could specifically recognize and be delivered into cancer cells to minimize the adverse effects on normal cells. To further confirm the contribution of CD44-mediated internalization, we pretreated the MDA-MB-231 cells with free HA to saturate the HA-CD44 binding, and then tested the cell uptake. In this case, the Ce6 fluorescence significantly weakened, demonstrating the critical role of HA modification for targeted delivery. The Ogura method was also performed to quantify the fluorescence, and the results were consistent with the CLSM observations (Fig. 3B)[48].

3.4. *Sensitizing photo/chemo-dynamic therapy and chemotherapy by MnO_2 doping*

Next, the *in vitro* tumor ablation activity was measured by MTT assay. As control experiments, the blank GO and GO@MH (without CisPt and Ce6 loading but with HA decoration) were examined. The cells maintained the viability with up to 200 μg/mL GO after 48 h incubation, indicating excellent biocompatibility of the nanocarrier (Fig. 4A). GO@MH, in contrast, showed moderate toxic effect at high concentration, which can be ascribed by the chemodynamic effect originated from the MnO_2 doping (Fig. 4A). Then, the MnO_2 sensitization for photo/chemo-dynamic therapy

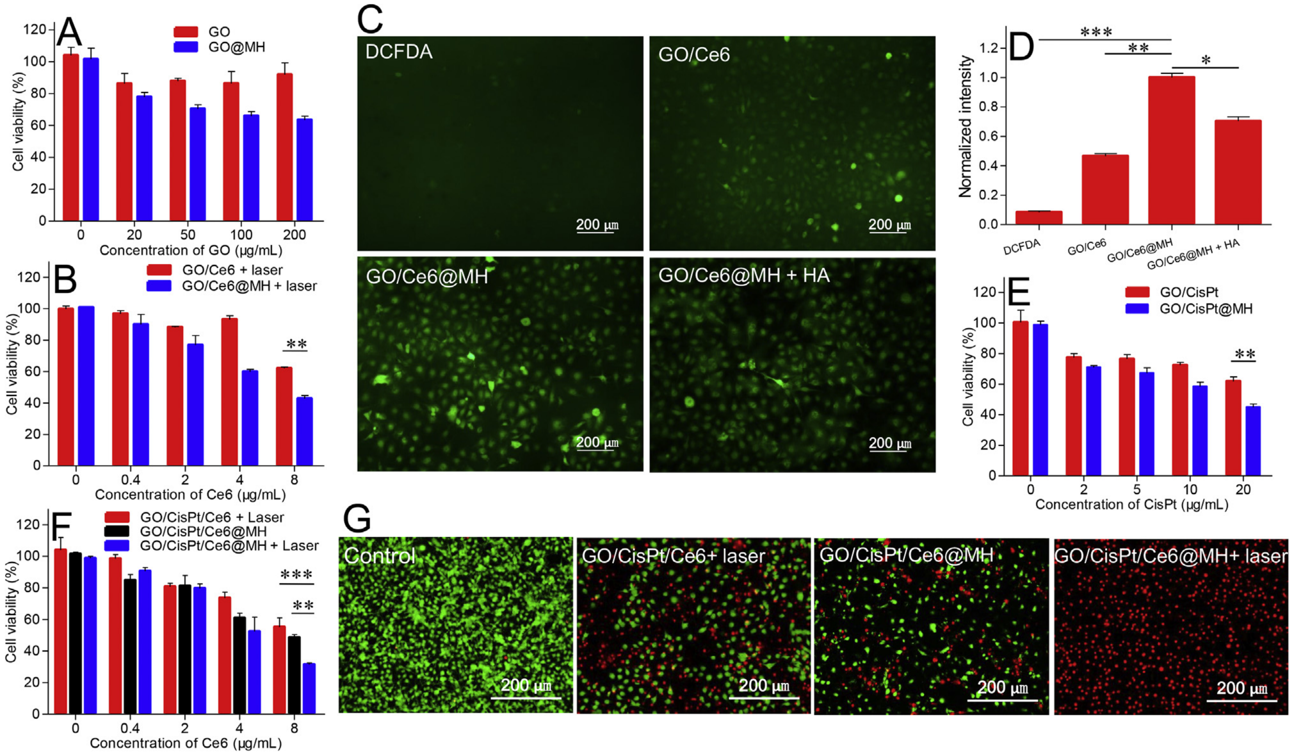

Figure 4 The viability of MDA-MB-231 cells detected by MTT assay after incubating with (A) drug-free carriers (GO and GO@MH). (B) GO/Ce6 and GO/Ce6@MH with 1 min laser (100 mW) irradiation for 48 h, $**P < 0.01$. (C) The fluorescence images of ROS by DCFDA staining in MDA-MB-231 cells treated with various formulations upon laser irradiation. The concentration of HA was 10 mg/mL. (D) The fluorescence quantitative analysis of ROS level inside cells. $*P < 0.05$, $**P < 0.01$, $***P < 0.001$. The cell viability after incubating with (E) GO/CisPt and GO/CisPt@MH (F) GO/CisPt/Ce6 + Laser, GO/CisPt/Ce6@MH and GO/CisPt/Ce6@MH + Laser. $**P < 0.01$, $***P < 0.001$. (G) The fluorescence images of MDA-MB-231 cells underwent different treatments co-stained by calcein-AM/PI. Data are expressed as mean ± SD ($n = 4$).

and chemotherapy were respectively studied. To test the enhanced photo/chemo-dynamic effect, Ce6-loaded GO was prepared (termed GO/Ce6), and further doped with MnO_2 to form GO/Ce6@MH. Upon exposure to light, both GO/Ce6 and GO/Ce6@MH showed a concentration-dependent toxicity, while at each concentration GO/Ce6@MH displayed considerably stronger cell damage than GO/Ce6 (Fig. 4B). There are several mechanisms to explain such enhanced anti-tumor effect, for example, the HA-mediated nanoparticles internalization and enhanced ROS generation by MnO_2. To specify each contribution, we also measured the intracellular ROS level by using 2′,7′-dichlorofluorescin diacetate (DCFDA) probe. DCFDA is non-fluorescent on its own, while it can be deacetylated and oxidized into fluorescent 2′,7′-dichloro-fluorescein (DCF) in presence of ROS, allowing for dynamic ROS monitoring by fluorescent signal. Quite weak fluorescence was observed in MDA-MB-231 cells without any treatment, indicating basal ROS level inside cells (Fig. 4C). Upon laser irradiation, both GO/Ce6 and GO/Ce6@MH showed effective ROS generation as indicated by much higher fluorescence. Based on fluorescence quantification (Fig. 4D), GO/Ce6@MH produced obviously stronger ROS. While free HA treatment decreased ROS generation to some extent, the resulting fluorescence was still higher than that of GO/Ce6 treating group. Therefore, both HA modification and MnO_2 decoration contribute to the enhanced ROS generation. Likewise, the enhanced chemotherapy was separated studied by conjugating CisPt on GO (termed GO/CisPt), and then adorning with MnO_2 to form GO/CisPt@MH. In this case, we also observed significantly intensified cytotoxicity for GO/CisPt@MH compared with GO/CisPt (Fig. 4E), confirming the sensitizing effect of MnO_2 for chemotherapy.

Finally, we investigated the therapeutic efficacy of GO/CisPt/Ce6@MH. After MnO_2 decoration and HA modification, the cytostatic activity of the multi-functional nanosystem was moderately improved compared to the GO/CisPt/Ce6 (with laser). Upon exposure to laser, the efficacy of GO/CisPt/Ce6@MH was further enhanced, suggesting a strong synergistic effect among each therapeutic modality (Fig. 4F). To clearly visualize synergistic effect, the cells were dual stained with calcein-AM and propidium iodide (PI) to identify the live (green) and dead cells (red), respectively (Fig. 4G). The cells without any treatment showed bright green fluorescence representing high viability. The red fluorescence became intensified with different treatment to indicate the cell damage effect, and the overall results were highly consistent with the MTT assays, further verifying the advantages of MnO_2 deposition.

3.5. *Potent tumor ablation in vivo*

Finally, we studied the *in vivo* anti-tumor efficacy of our designed system by using MDA-MB-231 tumor-bearing BALB/c mice. The mice were randomly divided into five groups ($n = 5$), each injected with 100 μL PBS (as control), GO/CisPt/Ce6 (with laser), GO/CisPt/Ce6@MH, and GO/CisPt/Ce6@MH (with laser), and the dose for Ce6 and CisPt was 0.5 mg/kg and 1.25 mg/kg, respectively. The laser irradiation was performed at 24 h after injection, and the therapeutic efficacy was recorded every other day by measuring the tumor size using a caliper. The control group with PBS treatment showed rapid tumor growth overtime (Fig. 5A). Interestingly, only marginal tumor inhibition was observed for GO/CisPt/Ce6 (with laser), likely due to the low drug dosages during our treatments. Without laser, the tumor ablation efficiency of GO/CisPt/Ce6@MH was also rather poor. This can be explained by that triple negative breast cancer is insensitive to the single treatment of CisPt[59]. Combined with laser irradiation, in contrast, a strong inhibitory effect was observed, in which the tumor growth was completely inhibited within 14 days, demonstrating the synergistic therapy of the nanoplatform. The therapeutic efficacy can be clearly observed from the photographs of mice after treatments (Fig. 5B, and Supporting Information Fig. S11), which showed remarkable tumor necrosis and ablation with GO/CisPt/Ce6@MH (with laser) treatment. The final outcome was evaluated by extracting the tumor tissue after treatment, and the GO/CisPt/Ce6@MH plus irradiation showed the most significant tumor ablation (Fig. 5C). Next, therapeutic efficacy was further studied by evaluating the tumor tissue using H&E staining assay. The tumor with PBS treatment showed large nuclei and spindle shapes, signifying the rapid cell growth (Fig. 5D). For GO/CisPt/Ce6 (with laser) and GO/CisPt/Ce6@MH-treating groups, the cell morphologies were moderately changed due to the limited therapeutic efficiency. However, GO/CisPt/Ce6@MH with irradiation induced the highest cell necrosis, indicating the enhanced therapeutic efficacy.

To confirm the critical functions of MnO_2 *in vivo*, we further measured the hypoxia inducible factor-1α (HIF-1α) and GSH levels in tumor tissues. Without any treatment, the tumor was featured with high level of HIF-1α, showing green immunofluorescent signal (Fig. 5E). After GO/CisPt/Ce6 (with laser) treatment, the HIF-1α expression was further enhanced, due to the

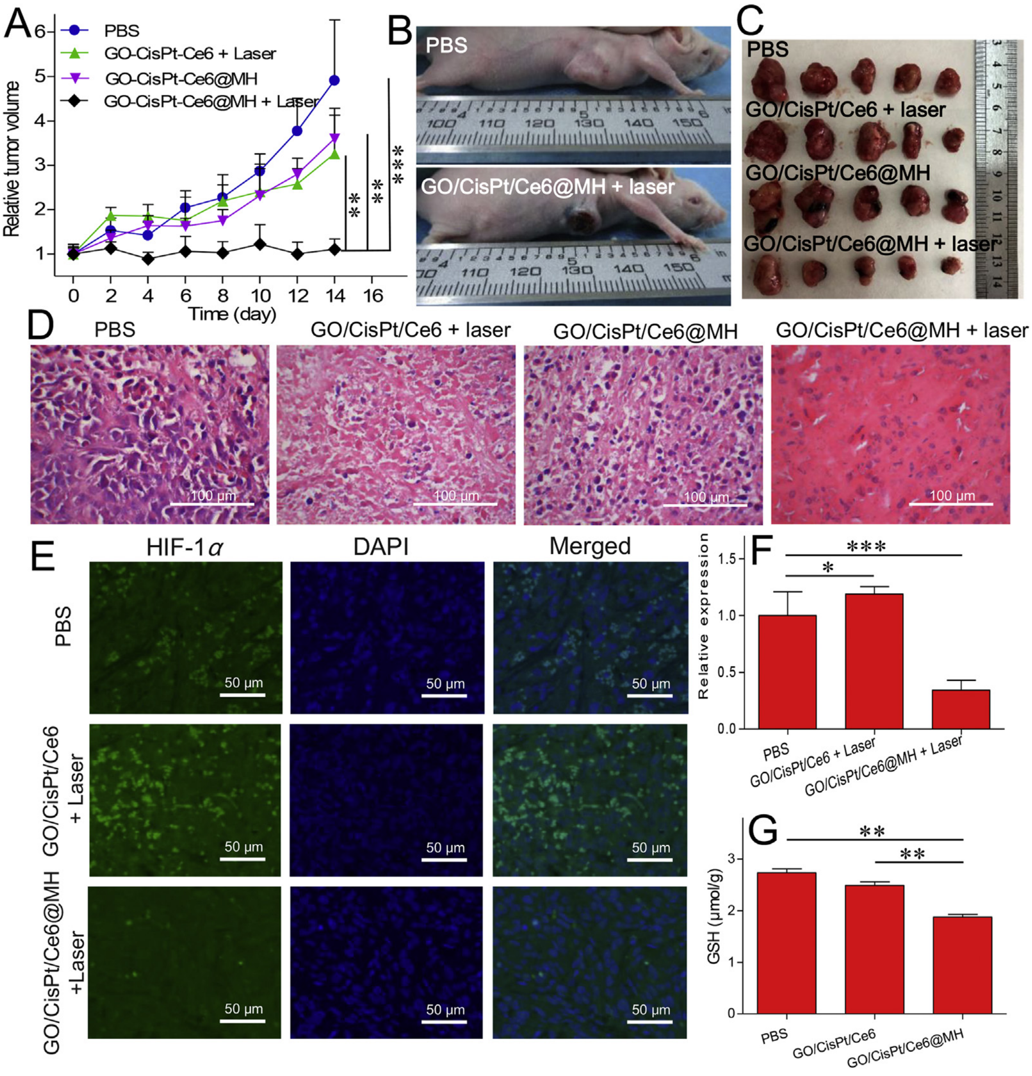

Figure 5 (A) Relative tumor volumes of the MDA-MB-231 tumor-bearing mice after different treatments over time. Data are expressed as mean ± SD ($n = 5$); $^{**}P < 0.01$, $^{***}P < 0.001$. (B) The photographs of mice after different treatments. (C) The tumor tissues collected on Day 14 after different treatments. (D) H&E staining images of the tumor tissues after different treatments. (E) The HIF-1α level in tumor tissue after various treatments measured by immunofluorescence assay. (F) The quantified HIF-1α level treated with different formulations. Data are expressed as mean ± SD ($n = 3$); $^{*}P < 0.05$, $^{***}P < 0.001$ (G) The GSH content in tumor tissue after various treatments. Data are expressed as mean ± SD ($n = 3$); $^{**}P < 0.01$.

oxygen consumption by photodynamic reaction that exacerbates the tumor hypoxia. However, when the tumor was treated with GO/CisPt/Ce6@MH (with laser), the HIF-1α expression was decrease by 66% (Fig. 5F), likely due to the O_2 generation in tumor catalyzed by MnO_2. In addition, the GSH depletion effect was also demonstrated by the significantly decreased tumor GSH content after GO/CisPt/Ce6@MH treatment as opposed to both PBS and GO/CisPt/Ce6 treating groups (Fig. 5G). Therefore, the MnO_2 can fulfil its roles *in vivo* to enhance anti-tumor activity by simultaneous self-oxygen supply and GSH depletion.

Finally, for the safety concern, the body weight of mice was measured and the major organs of mice (heart, liver, spleen, lung, and kidney) were harvested for H&E analysis to examine the systemic toxicity. No obvious decrease of body weight was observed for all groups (Supporting Information Fig. S12), and major organs did not exhibit significant damage, suggesting no short-term toxicity during treatment (Supporting Information Fig. S13). Therefore, the nanoplatform has excellent biocompatibility and efficient therapy against tumor.

4. Conclusions

In summary, we developed a CisPt and Ce6 dual-loaded GO/CisPt/Ce6@MH complex for enhanced chemo-photodynamic therapy with tumor targeted drug delivery. The key component of the nanosystem was the surface MnO_2 doping, which has been systematically characterized by TEM, AFM, XPS and elemental mapping. The multi-system depletion activity allowed the nanosystem to effectively regulate tumor microenvironment by simultaneously relieving tumor hypoxia and alleviating GSH-mediated resistance. With such merits, the key limitations for cancer treatment have been elegantly resolved. Combining the self-oxygen supply with effective GSH depletion, the GO/CisPt/Ce6@MH displayed a superior antitumor efficacy for tumor chemo-photodynamic therapy.

Acknowledgments

This work was supported by Innovation-Driven Project of Central South University (No. 20170030010004, China), National Natural Science Foundation of China (No. 21804144, U1903125, China), Project of Hunan Science and Technology (No. 2020JJ8091, China), and Hunan Engineering Research Center for Optimization of Drug Formulation and Early Clinical Evaluation (No. 2015TP2005, China).

Author contributions

Peng Liu, Jinsong Ding and Wenhu Zhou designed and conceptualized this study. Peng Liu, Miao Liu, Xin Xie and Shuo Hu performed the in *vitro* and in *vivo* experiments. Peng Liu, and Wenhu Zhou drafted the manuscript. All of the authors have read and approved the final manuscript.

Conflicts of interest

The authors have no conflicts of interest to declare.

Appendix A. Supporting information

Supporting data to this article can be found online at https://doi.org/10.1016/j.apsb.2020.07.021.

References

1. Nieboer P, de Vries EGE, Mulder NH, van der Graaf WTA. Relevance of high-dose chemotherapy in solid tumours. *Canc Treat Rev* 2005;**3**: 210−25.
2. Fan W, Yung B, Huang P, Chen X. Nanotechnology for multimodal synergistic cancer therapy. *Chem Rev* 2017;**22**:13566−638.
3. Shen B, Zhao K, Ma S, Yuan D, Bai Y. Topotecan-loaded mesoporous milica nanoparticles for reversing multi-drug resistance by synergetic chemoradiotherapy. *Chem Asian J* 2015;**2**:344−8.
4. Wu P, Wang XF, Wang ZD, Ma W, Guo JS, Chen JJ, et al. Light-activatable prodrug and AIEgen copolymer nanoparticle for dual-drug monitoring and combination therapy. *ACS Appl Mater Interfaces* 2019;**20**:18691−700.
5. Voon SH, Kiew LV, Lee HB, Lim SH, Noordin MI, Kamkaew A, et al. *In vivo* studies of nanostructure-based photosensitizers for photodynamic cancer therapy. *Small* 2014;**24**:4993−5013.
6. Huang P, Lin J, Wang S, Zhou Z, Li Z, Wang Z, et al. Photosensitizer-conjugated silica-coated gold nanoclusters for fluorescence imaging-guided photodynamic therapy. *Biomaterials* 2013;**19**:4643−54.
7. Han K, Wang SB, Lei Q, Zhu JY, Zhang XZ. Ratiometric biosensor for aggregation-induced emission-guided precise photodynamic therapy. *ACS Nano* 2015;**10**:10268−77.
8. Liu P, Xie X, Shi X, Peng Y, Ding J, Zhou W. Oxygen-self-supplying and HIF-1α inhibiting core-shell nano-system for hypoxia-resistant photodynamic therapy. *ACS Appl Mater Interfaces* 2019;**11**: 48261−70.
9. Zhang J, Jiang CS, Longo JPF, Azevedo RB, Zhang H, Muehlmann LA. An updated overview on the development of new photosensitizers for anticancer photodynamic therapy. *Acta Pharm Sin B* 2018;**2**:137−46.
10. Liu K, Liu X, Zeng Q, Zhang Y, Tu L, Liu T, et al. Covalently assembled NIR nanoplatform for simultaneous fluorescence imaging and photodynamic therapy of cancer cells. *ACS Nano* 2012;**5**: 4054−62.
11. Wang Q, Dai YN, Xu JZ, Cai J, Niu XR, Zhang L, et al. All-in-one phototheranostics: single laser triggers NIR-II fluorescence/photoacoustic imaging guided photothermal/photodynamic/chemo combination therapy. *Adv Funct Mater* 2019;**31**:12.
12. Xiao Y, An FF, Chen J, Xiong S, Zhang XH. The impact of light irradiation timing on the efficacy of nanoformula-based photo/chemo combination therapy. *J Mat Chem B* 2018;**22**:3692−702.
13. Tang XL, Jing F, Lin BL, Cui S, Yu RT, Shen XD, et al. pH-responsive magnetic mesoporous silica-based nanoplatform for synergistic photodynamic therapy/chemotherapy. *ACS Appl Mater Interfaces* 2018;**17**:15001−11.
14. Liu R, Yu M, Yang X, Umeshappa CS, Hu C, Yu W, et al. Linear chimeric triblock molecules self-assembled micelles with controllably transformable property to enhance tumor retention for chemo-photodynamic therapy of breast cancer. *Adv Funct Mater* 2019;**23**: 1808462.
15. Tian J, Xiao C, Huang B, Wang C, Zhang W. Janus macromolecular brushes for synergistic cascade-amplified photodynamic therapy and enhanced chemotherapy. *Acta Biomater* 2020;**101**:495−506.
16. Fang JF, Wang Q, Yang GJ, Xiao X, Li LC, Yu T. Albumin-MnO_2 gated hollow mesoporous silica nanosystem for modulating tumor

hypoxia and synergetic therapy of cervical carcinoma. *Colloids Surf B Biointerfaces* 2019;**179**:250−9.

17. Feng Y, Ding D, Sun W, Qiu Y, Luo L, Shi T, et al. Magnetic manganese oxide sweetgum-ball nanospheres with large mesopores regulate tumor microenvironments for enhanced tumor nanotheranostics. *ACS Appl Mater Interfaces* 2019;**41**:37461−70.
18. Brown JM, Wilson WR. Exploiting tumour hypoxia in cancer treatment. *Nat Rev Canc* 2004;**6**:437−47.
19. Liu L, Ruan Z, Li T, Yuan P, Yan L. Near infrared imaging-guided photodynamic therapy under an extremely low energy of light by galactose targeted amphiphilic polypeptide micelle encapsulating BODIPY-Br 2. *Biomater Sci* 2016;**11**:1638−45.
20. Dang J, He H, Chen D, Yin L. Manipulating tumor hypoxia toward enhanced photodynamic therapy (PDT). *Biomater Sci* 2017;**8**: 1500−11.
21. Kostenich G, Kimel S, Peled S, Orenstein A. Monitoring PDT-induced damage using spectrally resolved reflectance imaging of tissue oxygenation. *Canc Lett* 2005;**2**:169−75.
22. Sun Y, Zhao D, Wang G, Wang Y, Cao L, Sun J, et al. Recent progress of hypoxia-modulated multifunctional nanomedicines to enhance photodynamic therapy: opportunities, challenges, and future development. *Acta Pharm Sin B* 2020;**10**:1382−96.
23. Gao S, Wang G, Qin Z, Wang X, Zhao G, Ma Q, et al. Oxygen-generating hybrid nanoparticles to enhance fluorescent/photoacoustic/ultrasound imaging guided tumor photodynamic therapy. *Biomaterials* 2017;**112**:324−35.
24. Hu D, Chen L, Qu Y, Peng J, Chu B, Shi K, et al. Oxygen-generating hybrid polymeric nanoparticles with encapsulated doxorubicin and chlorin e6 for trimodal imaging-guided combined chemo-photodynamic therapy. *Theranostics* 2018;**6**:1558−74.
25. Cheng YH, Cheng H, Jiang CX, Qiu XF, Wang KK, Huan W, et al. Perfluorocarbon nanoparticles enhance reactive oxygen levels and tumour growth inhibition in photodynamic therapy. *Nat Commun* 2015;**1**:1−8.
26. Chen X, Liu Y, Wen Y, Yu Q, Liu J, Zhao Y, et al. A photothermal-triggered nitric oxide nanogenerator combined with siRNA for precise therapy of osteoarthritis by suppressing macrophage inflammation. *Nanoscale* 2019;**14**:6693−709.
27. Grivennikov SI, Greten FR, Karin M. Immunity, inflammation, and cancer. *Cell* 2010;**6**:883−99.
28. Stowe DF, Camara AK. Mitochondrial reactive oxygen species production in excitable cells: modulators of mitochondrial and cell function. *Antioxidants Redox Signal* 2009;**6**:1373−414.
29. Kavčič N, Pegan K, Vandenabeele P, Turk B. Comparative study of the differential cell death protecting effect of various ROS scavengers. *Biol Chem* 2019;**2**:149−60.
30. Moloney JN, Cotter TG. ROS signalling in the biology of cancer. *Semin Cell Dev Biol* 2018;**80**:50−64.
31. Kiesslich T, Plaetzer K, Oberdanner CB, Berlanda J, Obermair FJ, Krammer B. Differential effects of glucose deprivation on the cellular sensitivity towards photodynamic treatment-based production of reactive oxygen species and apoptosis-induction. *FEBS Lett* 2005;**1**: 185−90.
32. Hall MD, Hambley TW. Platinum (IV) antitumour compounds: their bioinorganic chemistry. *Coord Chem Rev* 2002;**1**:49−67.
33. Váradi A, Sarkadi B. Multidrug resistance-associated proteins: export pumps for conjugates with glutathione, glucuronate or sulfate. *Biofactors* 2003;**1**:103−14.
34. Mellish K, Kelland L, Harrap K. *In vitro* platinum drug chemosensitivity of human cervical squamous cell carcinoma cell lines with intrinsic and acquired resistance to cisplatin. *Brit J Cancer* 1993;**2**: 240−50.
35. Surnar B, Sharma K, Jayakannan M. Core−shell polymer nanoparticles for prevention of GSH drug detoxification and cisplatin delivery to breast cancer cells. *Nanoscale* 2015;**42**:17964−79.
36. Han Y, Yin W, Li J, Zhao H, Zha Z, Ke W, et al. Intracellular glutathione-depleting polymeric micelles for cisplatin prodrug delivery to overcome cisplatin resistance of cancers. *J Control Release* 2018;**273**:30−9.
37. Yang K, Feng L, Shi X, Liu Z. Nano-graphene in biomedicine: theranostic applications. *Chem Soc Rev* 2013;**2**:530−47.
38. Li J-L, Tang B, Yuan B, Sun L, Wang X-G. A review of optical imaging and therapy using nanosized graphene and graphene oxide. *Biomaterials* 2013;**37**:9519−34.
39. Liu J, Dong J, Zhang T, Peng Q. Graphene-based nanomaterials and their potentials in advanced drug delivery and cancer therapy. *J Control Release* 2018;**286**:64−73.
40. Luan X, Guan YY, Liu HJ, Lu Q, Zhao M, Sun D, et al. A tumor vascular-targeted interlocking trimodal nanosystem that induces and exploits hypoxia. *Adv Sci* 2018;**8**:1800034.
41. Liu J, Cui L, Losic D. Graphene and graphene oxide as new nanocarriers for drug delivery applications. *Acta Biomater* 2013;**12**: 9243−57.
42. Tian B, Wang C, Zhang S, Feng L, Liu Z. Photothermally enhanced photodynamic therapy delivered by nano-graphene oxide. *ACS Nano* 2011;**9**:7000−9.
43. Rong P, Yang K, Srivastan A, Kiesewetter DO, Yue X, Wang F, et al. Photosensitizer loaded nano-graphene for multimodality imaging guided tumor photodynamic therapy. *Theranostics* 2014;**3**: 229−39.
44. Liu P, Wang S, Liu X, Ding J, Zhou W. Platinated graphene oxide: a nanoplatform for efficient gene-chemo combination cancer therapy. *Eur J Pharmaceut Sci* 2018;**121**:319−29.
45. Dai Y, Wang B, Sun Z, Cheng J, Zhao H, Wu K, et al. Multifunctional theranostic liposomes loaded with a hypoxia-activated prodrug for cascade-activated tumor selective combination therapy. *ACS Appl Mater Interfaces* 2019;**43**:39410−23.
46. Wang M, Zhai Y, Ye H, Lv Q, Sun B, Luo C, et al. High co-loading capacity and stimuli-responsive release based on cascade reaction of self-destructive polymer for improved chemo-photodynamic therapy. *ACS Nano* 2019;**6**:7010−23.
47. Golla ED, Ayres GH. Spectrophotometric determination of platinum with *o*-phenylenediamine. *Talanta* 1973;**2**:199−210.
48. Ogura SI, Fujita Y, Kamachi T, Okura I. Preparation of chlorin e6-monoclonal antibody conjugate and its effect for photodynamic therapy. *J Porphyr Phthalocyanines* 2001;**5**:486−9.
49. Moore TL, Rodriguez-Lorenzo L, Hirsch V, Balog S, Urban D, Jud C, et al. Nanoparticle colloidal stability in cell culture media and impact on cellular interactions. *Chem Soc Rev* 2015;**17**: 6287−305.
50. Yang X, Yang Y, Gao F, Wei JJ, Qian CG, Sun MJ. Biomimetic hybrid nanozymes with self-supplied H^+ and accelerated O_2 generation for enhanced starvation and photodynamic therapy against hypoxic tumors. *Nano Lett* 2019;**7**:4334−42.
51. Zhang YH, Qiu WX, Zhang M, Zhang L, Zhang XZ. MnO_2 motor: a prospective cancer-starving therapy promoter. *ACS Appl Mater Interfaces* 2018;**17**:15030−9.
52. Ju E, Dong K, Chen Z, Liu Z, Liu C, Huang Y, et al. Copper (II)−graphitic carbon nitride triggered synergy: improved ROS generation and reduced glutathione levels for enhanced photodynamic therapy. *Angew Chem Int Ed* 2016;**38**:11639−43.
53. Fan H, Yan G, Zhao Z, Hu X, Zhang W, Liu H, et al. A smart photosensitizer−manganese dioxide nanosystem for enhanced photodynamic therapy by reducing glutathione levels in cancer cells. *Angew Chem Int Ed* 2016;**18**:5477−82.
54. Wang XQ, Gao F, Zhang XZ. Initiator-loaded gold nanocages as a light-induced free-radical generator for cancer therapy. *Angew Chem Int Ed* 2017;**31**:9029−33.
55. Gibson D. The mechanism of action of platinum anticancer agents-what do we really know about it?. *Dalton Trans* 2009;**48**:10681−9.

56. Lin LS, Song J, Song L, Ke K, Liu Y, Zhou Z, et al. Simultaneous fenton-like ion delivery and glutathione depletion by MnO_2-based nanoagent to enhance chemodynamic therapy. *Angew Chem Int Ed* 2018;**18**:4902−6.
57. Wang Q, Tian S, Ning P. Degradation mechanism of methylene blue in a heterogeneous fenton-like reaction catalyzed by ferrocene. *Ind Eng Chem Res* 2014;**2**:643−9.
58. Hu C, Cun X, Ruan S, Liu R, Xiao W, Yang X, et al. Enzyme-triggered size shrink and laser-enhanced NO release nanoparticles for deep tumor penetration and combination therapy. *Biomaterials* 2018:64−75.
59. Collignon J, Lousberg L, Schroeder H, Jerusalem G. Triple-negative breast cancer: treatment challenges and solutions. *Breast Cancer* 2016;**8**:93−107.